Object-based change detection from satellite imagery by segmentation optimization and multi-features fusion

Article *in* International Journal of Remote Sensing · July 2017

DOI: 10.1080/01431161.2017.1308033

2 authors:

Daifeng Peng
Wuhan University
6 PUBLICATIONS **7** CITATIONS

SEE PROFILE

Yongjun Zhang
Wuhan University
112 PUBLICATIONS **665** CITATIONS

SEE PROFILE

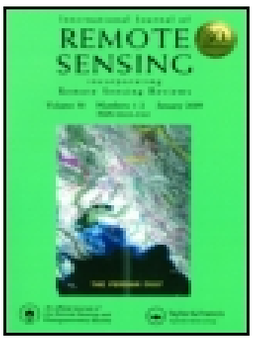

International Journal of Remote Sensing

ISSN: 0143-1161 (Print) 1366-5901 (Online) Journal homepage: http://www.tandfonline.com/loi/tres20

Object-based change detection from satellite imagery by segmentation optimization and multi-features fusion

Daifeng Peng & Yongjun Zhang

To cite this article: Daifeng Peng & Yongjun Zhang (2017) Object-based change detection from satellite imagery by segmentation optimization and multi-features fusion, International Journal of Remote Sensing, 38:13, 3886-3905, DOI: 10.1080/01431161.2017.1308033

To link to this article: http://dx.doi.org/10.1080/01431161.2017.1308033

Published online: 30 Mar 2017.

INTERNATIONAL JOURNAL OF REMOTE SENSING, 2017
VOL. 38, NO. 13, 3886–3905
http://dx.doi.org/10.1080/01431161.2017.1308033

Taylor & Francis
Taylor & Francis Group

Object-based change detection from satellite imagery by segmentation optimization and multi-features fusion

Daifeng Peng and Yongjun Zhang

School of Remote Sensing and Information Engineering, Wuhan University, Wuhan, Hubei, P.R. China

ABSTRACT

This article presents a novel object-based change detection (OBCD) approach in high-resolution remote-sensing images by means of combining segmentation optimization and multi-features fusion. In the segmentation optimization, objects with optimized boundaries and proper sizes are generated by object intersection and merging (OIM) processes, which ensures the accurate information extraction from image objects. Within multi-features fusion and change analysis, the Dempster and Shafer (D-S) evidence theory and the Expectation-Maximization (EM) algorithm are implemented, which effectively utilize multi-dimensional features besides avoiding the selection of an appropriate change threshold. The main advantages of our proposed method lie in the improvement of object boundary and the fuzzy fusion of multi-features information. The proposed approach is evaluated using two different high-resolution remote-sensing data sets, and the qualitative and quantitative analyses of the results demonstrate the effectiveness of the proposed approach.

ARTICLE HISTORY
Received 1 July 2016
Accepted 11 March 2017

1. Introduction

Remote-sensing change detection (CD) is the process of identifying the differences in the state of an object or natural phenomena by observing it at different times (Singh 1989). Natural surface CD is helpful in analysing vegetation growth while the detection of changes of artificial objects is useful in the management of natural resources and urban expansion monitoring. Remote-sensing imagery is widely used in CD research where the coverage areas are large, the revisit times are short, and the image information is abundant. CD is a significant tool in the field of land-use and land-cover investigation, resource surveying, urban expansion monitoring, environmental assessment, and rapid response to disaster events (Coppin et al. 2004; Lu et al. 2005; Hay et al. 2005; Gang and Hay 2011; Gong, Li, and Zhang 2013; Xu et al. 2015).

Numerous CD methods have been proposed by many researchers over the last few decades, which can be mainly divided into pixel-based and object-based methods (Nackaerts et al. 2005). In the pixel-based methods, the change features from two images are compared for each pixel independently. In the object-based methods, the

CONTACT Yongjun Zhang zhangyj@whu.edu.cn School of Remote Sensing and Information Engineering, Wuhan University, Wuhan, Hubei, P.R. China

images are segmented into disjoined and homogenous objects, from which their change features are extracted and compared. Pixel-based CD methods are mainly employed in medium- and low-resolution remote-sensing imagery. Many pixel-based CD techniques have been developed, including post-classification (Chang et al. 2010; Ghosh, Roy, and Ghosh 2014), change vector analysis (CVA) (Bruzzone and Prieto 2000; Nackaerts et al. 2005), principal component analysis (PCA) (Deng et al. 2008; Bao et al. 2012), and machine learning (Huang et al. 2008; Volpi et al. 2013; Cao et al. 2014). However, contextual information is ignored in pixel-based CD methods, which leads to lower CD accuracy and 'salt and pepper' noise. To overcome these drawbacks, the spatial-contextual information needs to be integrated to properly model the spatial properties of the scene to improve the CD accuracy. Spatial-context information can be introduced by kernels (Volpi et al. 2013), Markov Random Field and Conditional Random Field (Bruzzone and Prieto 2000; He et al. 2015; Cao, Zhou, and Li 2016), neighbouring windows (Celik 2009), neural networks (Ghosh et al. 2007), morphological filter (Falco et al. 2013), and hypergraph (Jian, Chen, and Zhang 2016).

With the ever-increasing spatial resolution, very-high-resolution (VHR) remote-sensing images tend to exhibit more scene details. With the traditional pixel-based CD methods, this increased variability in VHR images often results in too many changes being detected ('salt and pepper' noise). It is also difficult to model contextual information with pixel-based CD methods because the spatial relationships and arrangements of real-world objects are neglected. In addition, CD accuracy is highly dependent on the effectiveness of radiometric calibration and image registration. High-performance computing systems and efficient segmentation algorithms are providing greater ease of segmentation and feature extraction for VHR remote-sensing images, thereby enabling the implementation of object-based change detection (OBCD).

An object can be regarded as a set of pixels that are adjacent in space and spectrally similar to each other. There is abundant spectral, spatial, and shape information in an object (Möller, Lymburner, and Volk 2007). OBCD can effectively avoid the influence of 'salt and pepper' noise in VHR images by making full use of the contextual information and the abundant feature information. OBCD has become the main trend in the areas of VHR image CD and a great deal of progress has been made, which can be roughly categorized into three classes, namely feature-based object change detection (FOCD), classification-based object change detection (COCD), and hybrid change detection (HCD). (1) In FOCD, objects are generated by image segmentation, which is then followed by feature extraction (spectrum, texture, geometry, etc.), feature vector construction, and generation of a change map utilizing a similarity analysis of the feature vectors (Hall and Hay 2003; Bontemps et al. 2008; Tang, Zhang, and Huang 2011; Wang et al. 2015; Chen, Chen, and Jiang 2016; Yousif and Ban 2016). FOCD is an unsupervised CD method that can incorporate the latest computer vision and machine learning theory. Furthermore, object features and similarity measurements can be selected flexibly, making it the most studied OBCD method. (2) In COCD, the image objects are generated by image segmentation and then are classified using the object features. A change map is generated by a comparison and analysis of the class membership and geometry attributes of the objects (Xian and Homer 2010; Yang et al. 2012; Qin et al. 2013; Wu, Zhang, and Zhang 2016). Unlike the FOCD method, the COCD method possesses the ability to determine the change type of image objects; however, the CD

accuracy is highly dependent on the accuracy of the segmentation and classification, resulting in a lower CD overall accuracy (OA). (3) The HCD approach makes full use of the classification and feature extraction techniques for object detection. Then, a similarity measurement is introduced to determine the change information of the target (Li and Narayanan 2003; Qin et al. 2015; Xiao et al. 2016). The HCD method has the advantages of the former two methods and can achieve higher CD accuracy. However, HCD is complex and time-consuming and therefore is mainly applied to CD for a specific target (such as buildings, water areas, forests, etc.).

Despite all of the above advantages, since objects are of different sizes and shapes, OBCD results heavily depend on the accuracy of segmentation. Another challenge of OBCD is the requirement to select an appropriate change threshold in the mostly used FOCD methods. In traditional multi-temporal OBCD analysis, objects with the same geographical boundary must be generated first either by overlaying the vector data with the raster image (Lefebvre, Corpetti, and Hubert-Moy 2008) or by segmenting the multi-temporal images simultaneously as one new image (Conchedda, Durieux, and Mayaux 2008; Li et al. 2014). However, the influences of changes in the object's boundary and size are not fully considered by the above-mentioned methods. In particular, the object boundary in CD from different periods of images may differ greatly due to phenological or artificial changes, in which case a large number of missed alarms and false alarms may arise using the same object boundary. In addition, the increased variability present in VHR images reduces the spectral consistency and separability of the image objects, leading to considerable false alarms and missed alarms using only the spectral features in OBCD. Different visual features (spectrum, texture, gradient, shape, etc.) are complementary for image interpretation, and CD accuracy can be improved by integrating multi-features (Hegaratmascle and Seltz 2004; Du and Liu 2012; Chen, Chen, and Jiang 2016).

To address the aforementioned problems, a novel OBCD method is proposed in this article by combining segmentation optimization and multi-features fusion. First, watershed segmentation is implemented for each period of imagery to acquire the initial multi-temporal objects independently; second, the refined objects are generated based on the strategy of object intersection and merging (OIM); third, the spectral, spatial, and textual histogram features are extracted and the histogram heterogeneity is calculated by the *G*-statistic; finally, the Dempster and Shafer (D-S) theory and the Expectation-Maximization (EM) algorithm are applied for multi-features fusion and change analysis. The processing flow of the proposed method is shown in Figure 1. The remainder of this

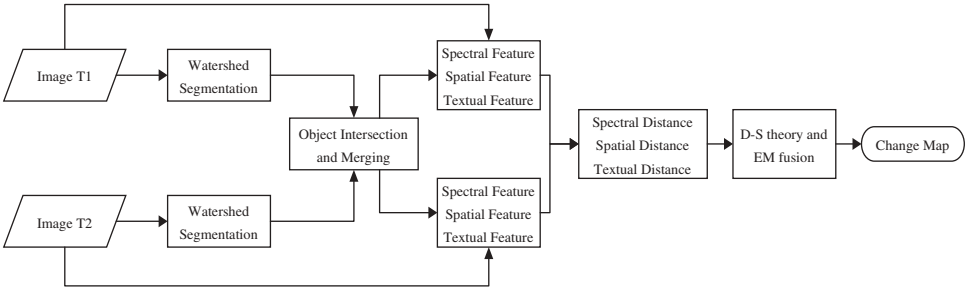

Figure 1. Flow chart of the proposed method.

article is organized as follows. Section 2 presents the proposed method in detail; the data set description and preprocessing are described in Section 3; the experimental results and analyses are illustrated in Section 4; and finally, Section 5 draws the conclusions.

2. Methodology

2.1. *Image segmentation and optimization*

Image segmentation is the basis of OBCD, whereby objects with intrinsic spectral consistency and spatial continuity are acquired. In our testing, a watershed segmentation algorithm (Hu et al. 2013) was applied to implement the multi-temporal independent segmentation, after which object intersection was carried out. Figure 2 shows the image segmentation and intersection results, where Figure 2(c) is the intersection result superimposed on image T1,

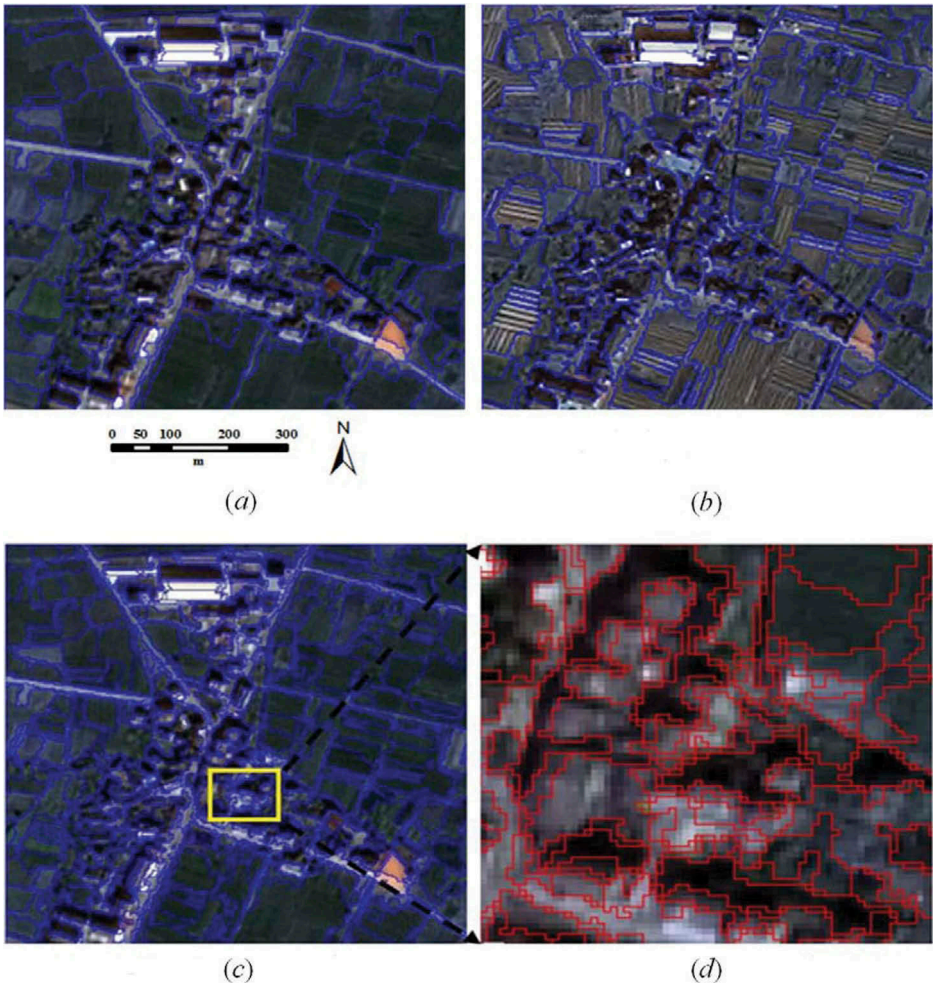

Figure 2. Image segmentation and intersection result: (a) segmentation result of image T1, (b) segmentation result of image T2, (c) intersection result superimposed on image T1, and (d) local result of (c).

and Figure 2(d) is the local magnification map. As can be seen from Figure 2(d), many small objects composed of only one or two pixels were produced, primarily at the edge of the segmentation results of two periods. In addition, due to some small remaining incorrect registrations or radiometric differences caused by seasonal or Sun angle changes, the object edges of the segmentation results from two different dates could not be matched perfectly (Tian et al. 2013). In particular, small objects composed of only a few pixels may lead to poor object statistical stability and the 'salt and pepper' effect to a large degree, which introduces considerable false alarms to the final results. Hence, proper object merging is required before performing further steps. To this end, a region merging strategy, which merges the small objects to their neighbouring larger objects based on the spectral consistency and spatial constraint, is employed to generate the final merging objects.

Let s be the scale, each small object R_s that must be merged is surrounded by several objects, which are hereafter referred to as candidate objects R_i (i = 1, 2, …, k, k is the total number of neighbours). The objective of this step is to merge the small objects into one of the candidate regions, which are larger but spectrally similar to the small objects. To achieve this objective, the similarity between the small objects and the candidate objects is measured, which is based on the difference map $D(x, y)$.

$$D(x,y) = \frac{1}{B}\sqrt{\sum_{i=1}^{B}\left(I_1^i(x,y) - I_2^i(x,y)\right)^2}, \tag{1}$$

where B is the number of bands, and $I_1^i(x,y)$ and $I_2^i(x,y)$ represent the pixel value at position (x,y) of the two periods of images, respectively. Merging a small object R_s into one candidate object R_i will produce a new object $R_i^{'}$. Generally speaking, merging that utilizes only spectral features can lead to meaningless objects with zigzag contours; therefore, it is necessary to incorporate them with the spatial features to improve the merging quality. We assume that the adjacent regions with a longer shared boundary and larger area should be merged with higher priority. Hence, we define the following heterogeneity function to measure the distance between $R_i >$ and $R_i^{'}$:

$$H_i = \frac{\left|\mu(R_i) - \mu(R_i^{'})\right|}{A^{\lambda_1} L^{\lambda_2}}, \tag{2}$$

where H_i represents the heterogeneity between R_i and $R_i^{'}$, $\mu(R_i) >$ and, *respectively*, $\mu\left(R_i^{'}\right)$ represent the mean grey value of R_i and $R_i^{'}$ in $D(x,y)$, A is the size of R_i, L is the length of the shared boundary of regions R_s and R_i, and λ_1 and λ_2 are defined as the parameters to adjust the area and shared boundary constraints. During the merging process, we define the size of the smallest object as the merge scale, and the merging process will iterate until the size of all of the regions is larger than the merge scale. The general procedure of the merging process is as follows.

Step 1: Set the merge scale s, initiate the merging state, and calculate the attributes (area, mean value, neighbours, and length of shared boundary) of every object.

Step 2: Traverse all the objects that are not merged; then, for each object smaller than s, merge it to its nearest neighbour calculated by Equation (2); finally, update the merging state and attributes.

Step 3: Repeat Step 2 until all the objects are larger than the merge scale.
Step 4: Generate the refined segmentation results.

The refined objects are generated after merging each small object into its candidate objects based on the above-mentioned merging process. As shown in Figure 3, small objects composed of a few pixels are merged into candidate objects and the object boundary becomes more consistent with the real boundary after merging.

2.2. *Feature extraction and distance measurement*

In this article, the spectral, spatial, and textual features are extracted and combined to improve the CD accuracy, where spectral features are delineated by the grey value of the pixel, spatial features are described using the gradient value of the pixel, and textual features are defined by Local Binary Pattern (LBP).

LBP is an effective texture description operator that utilizes a statistical analysis method, which was proposed and improved by Ojala (Ojala and Pietikäinen 1999). LBP is widely used in the areas of image analysis and object detection (residential area extraction, face detection, etc.) for its advantages of simple calculation and powerful texture description. LBP is computed using a 3×3 window, where the centre pixel serves as the threshold for the neighbourhood pixels segmentation, and the LBP value is obtained by convoluting with the same size of weight template, which is defined as follows:

$$\mathrm{LBP}_{P,R} = \sum_{p=0}^{P-1} 2^p s_p, \tag{3}$$

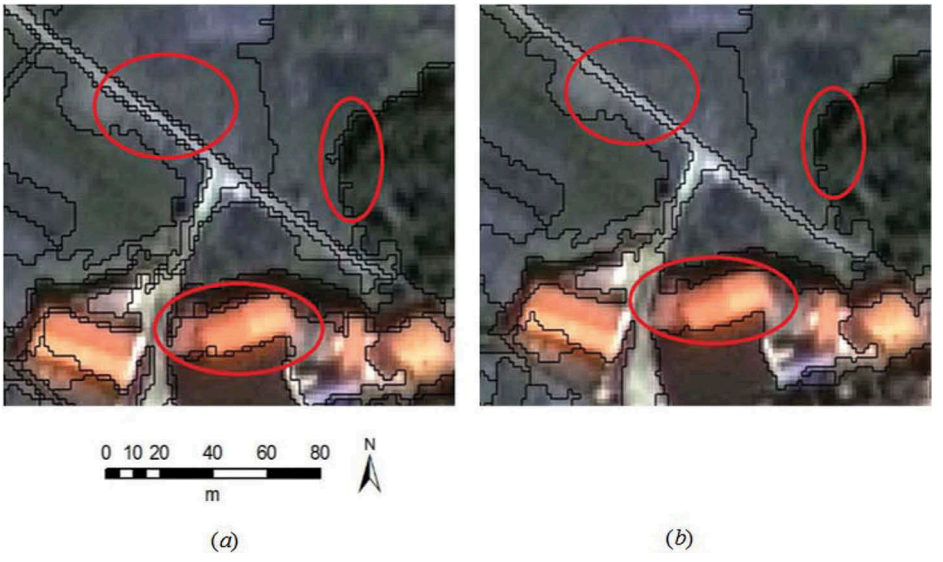

Figure 3. Object intersection and merging result: (a) intersection result and (b) merging result (the red ellipses denote the merging result of small objects).

$$s_p = s(g_p - g_c) = \begin{cases} 0 & g_p < g_c \\ 1 & g_p \geq g_c \end{cases}, \tag{4}$$

where P represents the number of pixels in the local window with a radius of R; g_p and g_c represent the grey values of the p-th neighbour and the centre pixel, respectively, and s_p is a binary flag denoting the relation of g_p and g_c. Figure 4 is a schematic diagram of LBP calculation. The original LBP is calculated with a fixed weight, making it sensitive to texture orientation. To overcome this problem, rotation-invariant LBP, namely LRI, is computed as proposed by Ojala (Ojala, Pietikäinen, and Mäenpää 2002), which is defined as follows:

$$\mathrm{LRI} = \frac{1}{P}\sum_{i=0}^{P-1} R(\mathrm{LBP}_{P,R}, i), \tag{5}$$

$$R(\mathrm{LBP}_{P,R}, i) = \begin{cases} \sum_{p=0}^{i-1} 2^{P-i+p} s_p + \sum_{p=1}^{P-1} 2^{P-i} s_p & 0 < i < P-1 \\ \mathrm{LBP}_{P,R} & i = 0 \end{cases}, \tag{6}$$

where $R\left(\mathrm{LBP}_{P,R}, i\right)$ represents the calculated LBP value after the i-th clockwise rotation of the weight template. For a 3×3 window, there are eight neighbourhoods and only 36 possible values for the rotation-invariant LBP. Local contrast (LC) portrays the magnitude of texture, which can be defined as follows:

$$\mathrm{LC}_{P,R} = \frac{T_1}{n_1} - \frac{T_2}{n_2}, \tag{7}$$

where T_1 represents the sum value of the brighter pixels in the window, n_1 is the number of brighter pixels, T_2 represents the sum value of the darker pixels in the window, and n_2 is the number of darker pixels. Both structure and magnitude information can be obtained by combining LBP and LC, which is of great importance for distinguishing different textures.

Moreover, the Sobel gradient is calculated to extract the object spatial features (Wahler and Shih 1989). After feature extraction, effective feature distances must be determined. In this method, the spectral distance of two regions is computed using their colour histograms, texture distance is calculated using the joint histograms of LBP and LC, and spatial distance is computed using gradient histograms. Meanwhile, to avoid making erroneous assumptions about feature distribution, the nonparametric statistical

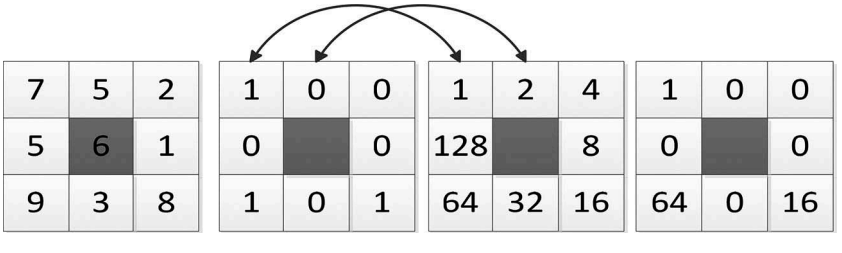

Figure 4. Scheme diagram of LBP and LC computation (LBP = 1 + 16 + 64 = 81; LC = (7 + 9 + 8)/3 − (5 + 2 + 5 + 1 + 3)/5 = 4.8).

method should be implemented to measure the distance of the two distributions of histograms. The *G*-statistic (Ojala, Pietikäinen, and Mäenpää 2002), which is a modification of the Kullback–Leibler distance, is used to measure the distance of the two histograms in this article.

Let B be the image band number and L be the grey level. Meanwhile, let $f_i^b(b = 1, 2, \ldots, B)$ be the frequency of grey value i in the object on band b. Hence, the distance of two histograms t_1 and t_2 on band b can be calculated as follows:

$$G^b = 2\left\{ \sum_{t_1,t_2} \sum_{i=0}^{L-1} f_i^b \ln\left(f_i^b\right) - \sum_{t_1,t_2} \left(\sum_{i=0}^{L-1} f_i^b \right) \ln\left(\sum_{i=0}^{L-1} f_i^b \right) - . \right.$$
$$\left. \sum_{i=0}^{L-1} \left(\sum_{i=0}^{L-1} f_i^b \right) \ln\left(\sum_{t_1,t_2} f_i^b \right) + \left(\sum_{t_1,t_2} \sum_{i=0}^{L-1} f_i^b \right) \ln\left(\sum_{t_1,t_2} \sum_{i=0}^{L-1} f_i^b \right) \right\} \tag{8}$$

The cumulative frequency is equal to 1 for each object; thus

$$\left. \begin{array}{c} \sum_{t_1,t_2} \left(\sum_{i=0}^{L-1} f_i^b \right) \ln\left(\sum_{i=0}^{L-1} f_i^b \right) = 0 \\ \left(\sum_{t_1,t_2} \sum_{i=0}^{L-1} f_i^b \right) \ln\left(\sum_{t_1,t_2} \sum_{i=0}^{L-1} f_i^b \right) = 2 \ln 2 \end{array} \right\}. \tag{9}$$

By substituting Equation (8) into Equation (7), we can obtain Equation (9):

$$G^b = 2\left\{ \sum_{t_1,t_2} \sum_{i=0}^{L-1} f_i^b \ln\left(f_i^b\right) - \sum_{i=0}^{L-1} \left(\sum_{t_1,t_2} f_i^b \right) \ln\left(\sum_{t_1,t_2} f_i^b \right) + 2\ln 2 \right\}. \tag{10}$$

The amount of information in a single band image can be measured by image entropy. To make full use of the band information, the band's weighted value using the entropy value of each band is calculated and defined as follows:

$$\omega_b = \frac{E(b)}{\sum_{i=1}^{B} E(i)}. \tag{11}$$

Finally, for each object we can compute the object homogeneity H_f, which can be defined as follows:

$$H_f = \sum_{b=1}^{B} \omega_b G^b. \tag{12}$$

2.3 *Feature fusion by the D-S theory and the EM algorithm*

The D-S evidence theory is a mathematical tool for uncertainty modelling and reasoning, which considers both objectivity and subjectivity of the evidence in probability reasoning. The probability of the evidence theory is the belief of a proposition based on the evidence. The theory implements induction and estimation based on multi-source information, from which a correct decision can be drawn (Ruthven and Lalmas 2002).

In the D-S theory, let Θ be the frame of discernment, then the power set of Θ is denoted by 2^{Θ}. The probability mass $m(\mathrm{A})$ is assigned to every class $\mathrm{A}\epsilon 2^{\Theta}$ by a sensor, such that $0 \leq m(\mathrm{A}) \leq 1$, $m(\phi) = 0$, and $\sum_{\mathrm{A}\in 2^{\Theta}} m(\mathrm{A}) = 1$, where ϕ denotes the empty set.

The D-S theory combines the different evidence with an orthogonal sum. If the p sources are available and we let $m_1, m_2, m_3 \ldots m_p$ be the corresponding probability masses, their orthogonal sum is denoted as follows:

$$m = m_1 \oplus m_2 \oplus \ldots \oplus m_p, \tag{13}$$

and the combined mass for each class $\mathrm{A}\epsilon 2^{\Theta}$can be defined as follows:

$$m(\mathrm{A}) = \frac{\sum_{\cap A_i = \mathrm{A}} \prod_{1 \leq j \leq p} m_j(A_i)}{1 - \sum_{\cap A_i = \phi} \prod_{1 \leq j \leq p} m_j(A_i)}. \tag{14}$$

In this article, the discernment frame $\Theta = \{\mathrm{Y}, \mathrm{N}\}$, where Y represents the changed class and N is the unchanged classes. The non-empty subsets of 2^{Θ} are {Y}, {N}, {Y, N}. Then, the probability mass for each non-empty subset can be created with Equation (15):

$$\begin{cases} m_i(\{\mathrm{Y}\}) = P_i \alpha_i \\ m_i(\{\mathrm{N}\}) = (1.0 - P_i)\alpha_i \\ m_i(\{\mathrm{Y}, \mathrm{N}\}) = 1.0 - \alpha_i \end{cases} \qquad i = 1, 2, 3, \tag{15}$$

where P_i is the probability masses computed from the spectral, textural, and spatial features, and α_i is the trust degree of evidence to the discernment frame. Finally, by implementing the evidence fusion with Equation (14) to calculate $m(\{\mathrm{Y}\})$, $m(\{\mathrm{N}\})$, and $m(\{\mathrm{Y}, \mathrm{N}\})$, the changed and unchanged classes can be distinguished.

A heuristic approach is used for modelling the probability masses $P_i(x)$ for the homogeneity of the three features. In this article, the task is to classify each object into the changed class or unchanged class using the feature histogram distance; each feature is a cue to separate the subsets of Θ in our classification scheme. Let C_1 be the changed class and C_2 be the unchanged class; for the input parameters x smaller than a threshold t_1, we assume that the assignment of an object to class C_1 is very unlikely, which is modelled by a small probability mass P_1. Meanwhile, if the input parameter x is larger than a threshold t_2 with $t_1 < t_2$, we assume that the assignment of an object to class C_1 is quite certain, which is then modelled by a rather larger probability mass P_2 with $0 \leq P_1 < P_2 \leq 1$. If the input parameter x is between t_1 and t_2, a cubic parabola with horizontal tangents is used to avoid step edges, which is defined as follows:

$$P_i(x) = \begin{cases} P_1 & \text{if } x \leq t_1 \\ P_1 + (P_2 - P_1)\left[3\left(\frac{x - t_1}{t_2 - t_1}\right)^2 - 2\left(\frac{x - t_1}{t_2 - t_1}\right)^3\right] & \text{if } t_1 < x < t_2 \\ P_2 & \text{if } x \geq t_2 \end{cases}. \tag{16}$$

Assuming the information from each feature is never 100% certain, we use $P_1 = 0.05$ and $P_2 = 0.95$, which fully considers the feature information contradiction and random variation.

$t_1$and t_2 are, respectively, the low and high thresholds to classify each object, which are determined by experience in most algorithms (Rottensteiner et al. 2005). However,

the precision is not satisfying. In this article, all the values of object heterogeneity make up a set $H = \{h_1, h_2, \ldots h_i \ldots, h_N\}$, N is the number of objects; and h_i represents the heterogeneity of the i-th object. The elements in the set H are divided into two classes: changed and unchanged. The heterogeneity values of the object histogram corresponding to the changed class are large, while the values of the unchanged class are small. In this article, the elements in set H are assumed to be a Gaussian mixture distribution composed of two Gaussian components, which are defined as follows:

$$p(h_i) = p(\omega_c)p(h_i|\omega_c) + p(\omega_n)p(h_i|\omega_n) \quad i = 1, 2, ..., N, \tag{17}$$

$$p(h_i|\omega) = \frac{1}{\sqrt{2\pi}\delta_\omega}\exp\left(-\frac{(h_i - \mu_\omega)^2}{2\delta_\omega^2}\right)\omega \in \{\omega_c, \omega_n\}, \tag{18}$$

where ω_c and ω_n represent the changed objects and unchanged objects, respectively; $p(\omega_c)$ and $p(\omega_n)$denote the proportions of changed objects and unchanged objects, respectively; $p(\omega_c) + p(\omega_n) = 1; \mu_\omega$ is the mean value of the objects; and δ_ω is the standard deviation of the objects.

Therefore, t_1 and t_2 can be calculated from μ_ω and δ_ω, which is defined as follows:

$$\begin{cases} t_1 = \mu_{\omega_n} + k\delta_{\omega_n} \\ t_2 = \mu_{\omega_c} + k\delta_{\omega_c} \end{cases}, \tag{19}$$

where $\mu_{\omega_n}$and μ_{ω_c} are the mean values of the unchanged objects and changed objects, respectively; δ_{ω_n} and δ_{ω_c} are the standard deviation of the unchanged objects and changed objects, respectively; and k is the adjustment coefficient, $k \in [-2, 2]$.

Based on the above-mentioned assumptions, the problem of determining t_1 and t_2 is transformed into the process of estimating and solving the parameters of μ_ω and δ_ω and therefore is a parameter-solving problem with missing data due to the unknown change class of each object. In this article, the EM algorithm (Bruzzone and Prieto 2000) is employed to estimate the parameters of the Gaussian mixture distribution because it is an effective unsupervised estimation method that can find the local maximum likelihood value in missing data.

3. Data set description and preprocessing

3.1. *Study area and data*

Our proposed method was applied to two multi-temporal remote-sensing image data sets. The first data set contained two periods of Systeme Probatoire d'Observation de la Terre 5 (SPOT-5) multi-spectral images comprising three bands of Red, Green, and Near-Infrared with a spatial resolution of 2.5 m acquired over the region of Guangzhou City, China, in October 2006 and again in October 2007. The region is a 1239 × 923pixels area containing roof, vegetation, bare land, and road objects; the remarkable changes are the alterations of land cover. The corresponding images are shown in Figure 5(a-b). The second data set was a pair of Gaofen 1 (GF-1) multi-spectral fusion images comprising four bands of Red, Green, Blue, and Near-Infrared with a spatial resolution of 2 m acquired over Huangyan Country of Zhejiang Province, China, in November 2013 and again in January 2015. The region is a 1242 × 1086pixels area containing roof,

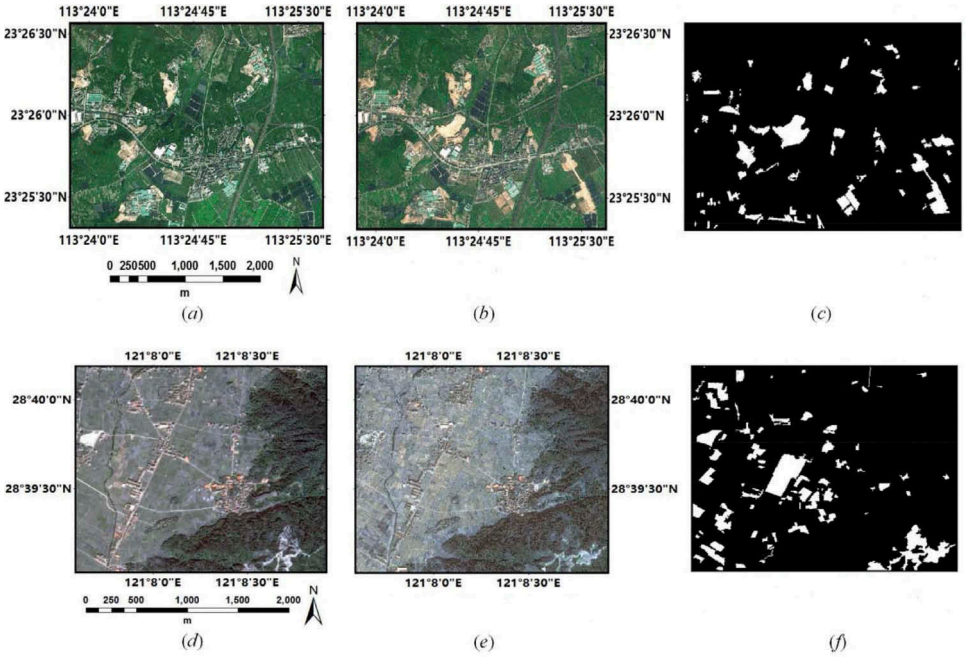

Figure 5. An illustration of two data sets for testing. (a), (b), and (c) represent the input multi-temporal images and reference change map of the Guangzhou data set, respectively; (d), (e), and (f) represent the input multi-temporal images and reference change map of the Huangyan data set, respectively; the changes are marked in white for each reference change map.

vegetation, bare land, field land, road, and forest objects. The main changes are the transitions of land cover, which is illustrated in Figure 5(d-e).

For each testing data set, a reference change map was prepared for qualitative evaluation purposes, which was manually generated according to a detailed visual interpretation as shown in Figure 5. Four metrics were used to permit a quantitative evaluation of the change results: (1) the false alarm (FA) rate, which is the number of unchanged pixels incorrectly detected as changed pixels over the total number of unchanged pixels; (2) the missed alarm (MA) rate, which is the number of changed pixels detected as unchanged pixels over the total number of changed pixels; (3) the OA, which is the total number of correctly detected pixels over the total number of pixels; and (4) the kappa coefficient (Foody 2004).

3.2. *Preprocessing*

Owing to the differences in illumination, Sun angle, and atmospheric conditions, image registration and radiometric normalization are of great importance when performing land-cover CD between images acquired on different dates. In this article, the multi-temporal images were automatically co-registered with the algorithm developed by Zhang et al. (2011). The root mean square error (RMSE) of registration was less than 0.5 pixels. The relative radiometric correction was implemented by applying the pseudo-invariant feature (PIF) method, which is more beneficial for CD compared with other relative radiometric correction methods because it minimally influences the original spectral values (Lo and Yang 2000).

4. Experiment and analysis

To validate the effectiveness of the proposed method, three experiments for each data set were designed and conducted.

4.1. *Experiment 1*

The first experiment investigated the impact of the merging scale on the CD accuracy. We varied the merging scale from 40 to 130 and computed the OA of the CD results. Figure 6 displays the results obtained for the two data sets. The OA values increased with the increase of merging scale at first, then decreased as the merging scale became larger. The optimal merging scales for the Guangzhou data set and the Huangyan data set were 70 and 60, respectively, which indicated that the optimal merging scale was data-independent.

4.2. *Experiment 2*

In order to analyse the effectiveness of the proposed segmentation optimization strategy on the performance of CD, we compared our proposed method with the two commonly used remote-sensing images segmentation strategies. (1) Segmentation was implemented on one period of image, then the generated object boundaries were simply assigned to the image acquired during the other period (Niemeyer, Marpu, and Nussbaum 2008). This strategy is regarded as single-temporal segmentation (STS). (2) All the bands of two periods of images were stacked for segmentation (Desclée, Bogaert, and Defourny 2006; Li et al. 2014), which is called multi-temporal combined segmentation (MTS). In this article, the optimal segmentation scale was determined using the Global Score (GS), which considers both global intra-segment goodness and inter-segment global goodness (Johnson and Xie 2011). In our proposed method (object intersection and merging with D-S theory fusion, OIM_DSF), the merging scale was set at 60, $\lambda_1 = 0.35$, $\lambda_2 = 0.65$. Then, the spectral, spatial, and texture features were extracted, and the D-S theory and EM algorithm (DS-EM) were implemented for change analysis, where $\alpha_1 = 0.95$, $\alpha_2 = 0.90$, and $\alpha_3 = 0.90$. Figure 7 shows the change maps produced by all of the tested methods, and Table 1 reports the quantitative results.

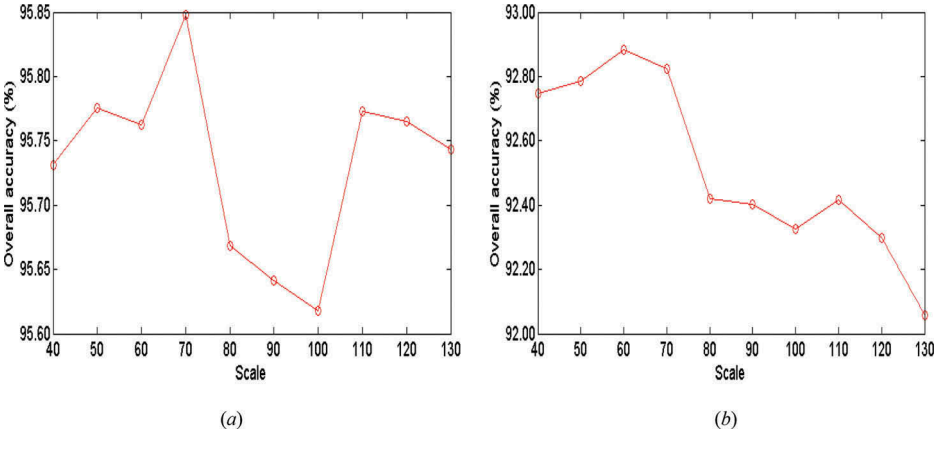

Figure 6. CD accuracy (overall accuracy rate values (%)) versus merging scale: (a) the Guangzhou data set and (b) the Huangyan data set.

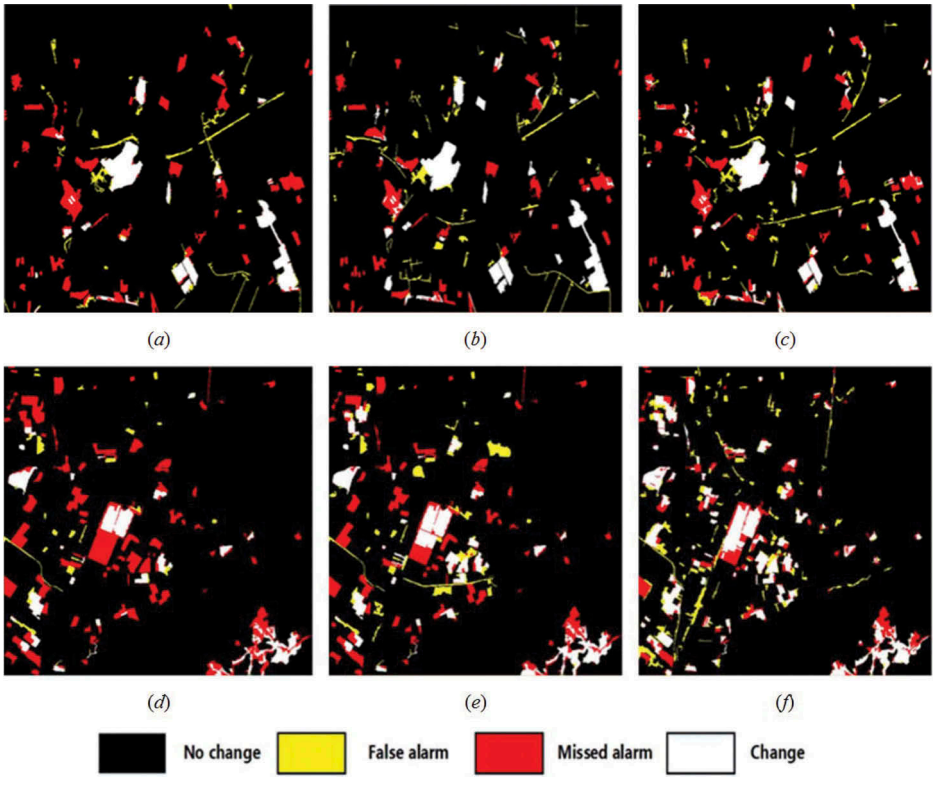

Figure 7. The CD results of the testing data sets. (a), (b), and (c) indicate the CD results obtained by STS, MTS, and OIM_DSF, respectively, in the Guangzhou data set; (d), (e), and (f) indicate the CD results obtained by STS, MTS, and OIM_DSF, respectively, in the Huangyan data set. The white areas in the images are the changed areas while the black areas are the unchanged ones; the yellow areas are the false alarms and the red areas are the missed alarms.

As can be seen from the above results, our proposed method performed the best on both data sets, which confirmed its superior capabilities and accuracy. The kappa coefficient using the STS method was lower than with the MTS method, and our proposed method achieved the highest kappa coefficient for both data sets. These results may be due to the fact that the STS method only considers one period of image for segmentation, and the object boundary may not be suitable for the other period of the image, especially when the image objects had changed. In the MTS method, two periods of images were used for segmentation, in which case the object boundary would be more suitable for both periods of images even when changes occurred. However, small objects were produced even at the optimal segmentation scale, which can seriously influence the statistical stability of the segmented objects and the calculated feature distances may not be accurate. Figure 8 shows the segmentation results of the different methods, where the regions in yellow circles denote the changed areas. We can see that the boundary in the area generated by the STS method was only suitable for image T2, but the boundary was suitable for both periods of the images utilizing the MTS method and our proposed method. In addition, as illustrated in Figure 9, there are many objects with areas less than 60 in both data sets with MTS,

Table 1. Summary of the quantitative evaluations for different segmentation strategies on the Guangzhou data set and the Huangyan data set (the bold numbers denote the best results).

	Guangzhou data set			Huangyan data set		
Method	STS	MTS	OIM_DSF	STS	MTS	OIM_DSF
MA (%)	28.64	26.53	**24.13**	30.75	29.31	**27.08**
FA (%)	5.13	5.52	**5.37**	5.92	6.35	**6.26**
OA (%)	92.95	93.91	**95.85**	90.41	91.36	**93.88**
kappa	0.48	0.52	**0.67**	0.42	0.45	**0.53**

while all the object areas are above 60 with our proposed method. Furthermore, the intersection operation with our proposed method produced objects where the object changes were fully considered. Based on the object size, the spectral difference, and the length of the shared boundary, the refined objects were generated by merging, where the sizes of all the segmented objects were above the defined scale. Therefore, the proposed method achieved better CD results.

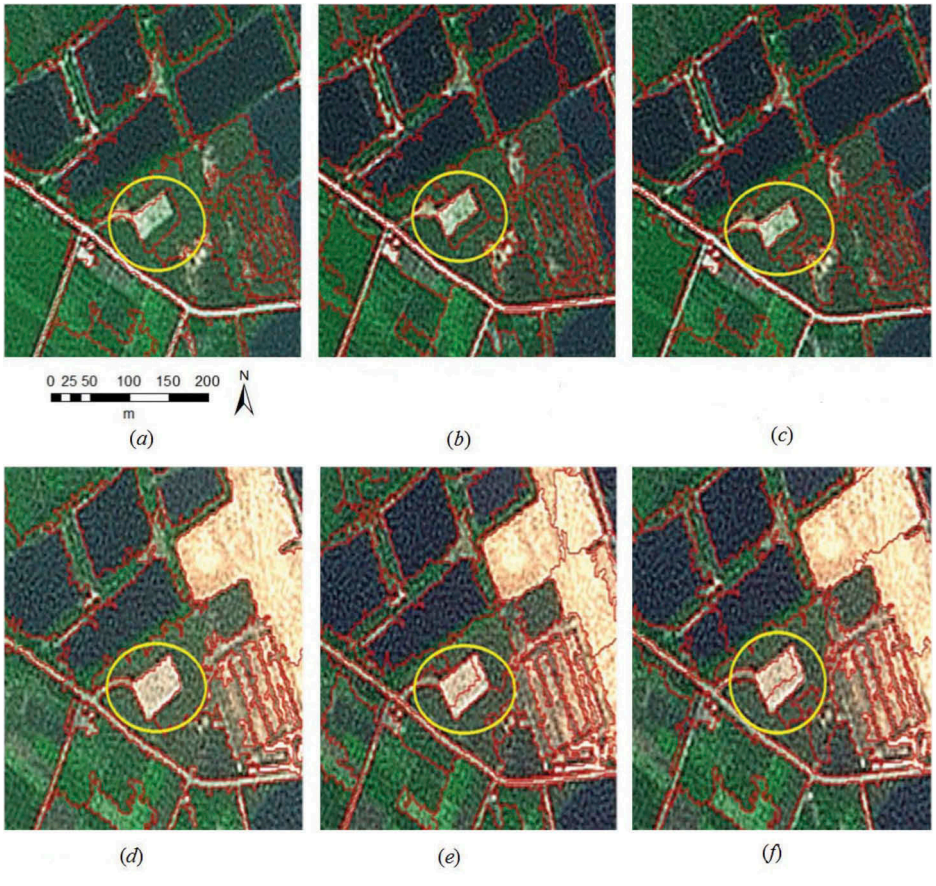

Figure 8. Illustration of segmentation results of the testing methods. (a), (b), and (c) indicate the segmentation results obtained by STS, MTS, and OIM_DSF, respectively, on image T1; (d), (e), and (f) indicate the segmentation results obtained by STS, MTS, and OIM_DSF, respectively, on image T2.

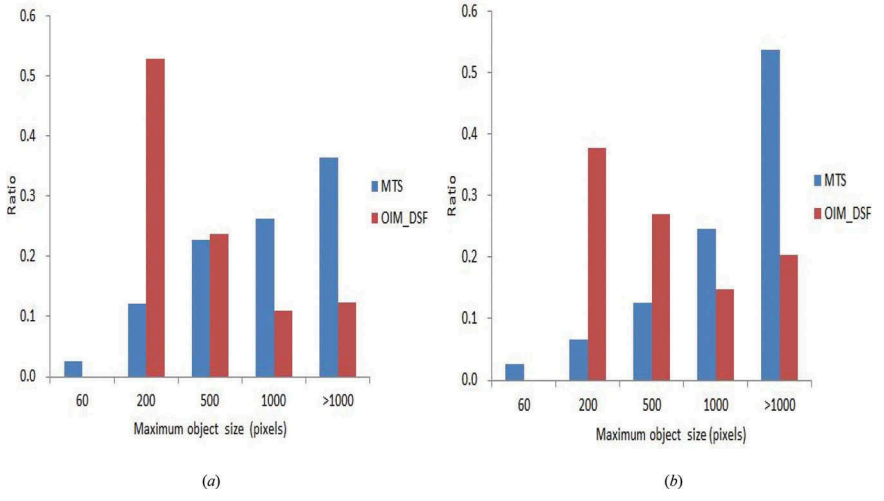

Figure 9. Object size distribution of two data sets: (a) the Guangzhou data set and (b) the Huangyan data set.

4.3 *Experiment 3*

In the third experiment, we assessed the effectiveness of the proposed multi-features fusion CD by comparing with two other forms of multi-features fusion CD methods: (1) a fuzzy set fusion (FSF) for the CD method, where fuzzy set theory is used for fusing different change information in multidimensional feature space in order to reduce the inconsistency of the CD results from different features (Wang, Wang, and Jiao 2010) and (2) a Support Vector Machine classification-based fusion (SVMF) for the CD method, which takes advantages of Support Vector Machine (SVM) in two-class separation in high-dimensional feature space (Mountrakis, Im, and Ogole 2011). In FSF, the EM algorithm was used to determine the optimal segmentation threshold in every difference feature band, and the sigmoid fuzzy membership function was applied for probability degree calculation, then fuzzy weighted fusion was performed according to the obtained class probability degrees. In SVMF, the Radial Basis Function (RBF) kernel was selected, and the two parameters C and γ were adaptively selected according to the two-dimensional grid searching strategy; then SVM classification was implemented using the selected training samples. The parameters of the proposed method were the same as in Experiment 2. Figure 10 shows the change maps produced by all of the methods above, and Table 2 illustrates the quantitative results.

According to the experiments, our proposed method obtained satisfactory results for both data sets. Both OA and kappa coefficient were very high with the proposed method, which validates its effectiveness and superior capabilities. Compared with the FSF method, the kappa coefficient was increased by 0.10 in the Guangzhou data set and 0.05 in the Huangyan data set, which indicates the superiority of the proposed multi-features fusion method. Our proposed method produced improved results mainly because the feature weights in FSF are determined by classification and therefore heavily depend on classification accuracy, whereas our proposed method does not require a complex weight calculation

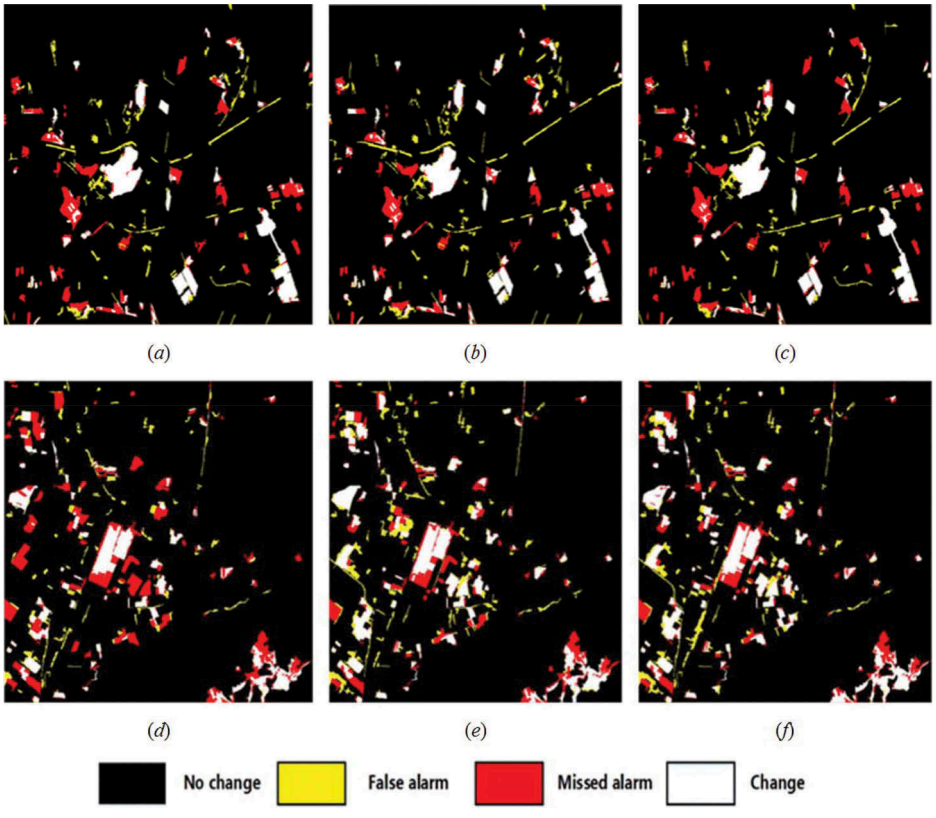

Figure 10. The CD results of the testing data sets. (a), (b), and (c) indicate the CD results obtained by FSF, SVMF, and OIM_DSF, respectively, in the Guangzhou data set; (d), (e), and (f) indicate the CD results obtained by FSF, SVMF, and OIM_DSF, respectively, in the Huangyan data set. The white areas in the images are the changed areas while the black areas are the unchanged ones; the yellow areas are the false alarms and the red areas are the missed alarms.

Table 2. Summary of the quantitative evaluations for different multi-features fusion methods on the Guangzhou data set and the Huangyan data set (the bold numbers denote the best results).

	Guangzhou data set			Huangyan data set		
Method	FSF	SVMF	OIM_DSF	FSF	SVMF	OIM_DSF
MA (%)	25.34	**23.72**	24.13	28.63	27.45	**27.08**
FA (%)	5.43	**5.38**	5.37	6.14	6.52	**6.26**
OA (%)	94.96	**96.32**	95.85	92.16	92.87	**93.88**
kappa	0.57	**0.69**	0.67	0.48	0.51	**0.53**

process. However, compared to the SVMF method, the proposed method obtained a lower kappa coefficient for the Guangzhou data set and a higher kappa coefficient for the Huangyan data set. The reason for these results may be that the supervised SVM classifier can effectively discriminate multiple information sources within the change class and can integrate the descriptions of changed objects from multiple features to realize the optimization of the output result. However, the classification process is highly dependent on the training samples, which are quite difficult to select when the scene is complex and the process is time-

consuming. This may explain why our proposed method achieved better performance than the SVMF method on the Huangyan data set, which is a more complex scene. Overall, in terms of accuracy and efficiency, our proposed method was found to be more effective and stable than the other two methods on both data sets.

5. Conclusion

In this article, we proposed a novel OBCD method by combining segmentation optimization and multi-features fusion using the D-S theory and EM algorithm. Objects with both an optimized boundary and a proper size were generated by the proposed OIM process, which reduced the influence of segmentation on the CD. The spectral, spatial, and textual histogram features were extracted and the feature distances were measured by the nonparametric *G*-statistic. The DS-EM method then was utilized for multi-features fusion, and change maps were generated using probability masses, thereby avoiding the process of selecting the change threshold and improving the CD accuracy. The performance of our proposed method was validated using real-world images generated by different sensors acquired in two different areas. The effectiveness of our proposed method was confirmed by comparing it with other reference methods qualitatively and quantitatively. The OIM method can achieve optimal segmentation, whereas multi-features fusion, by employing the fully automatic DS-EM method, achieves high accuracy and efficiency. From our experiments, we conclude that OBCD accuracy can be improved by combining the two methods. Further work may include investigating how to fuse more features (height, shape, etc.) effectively to further improve CD accuracy.

Disclosure statement

No potential conflict of interest was reported by the authors.

Funding

This work was supported by the National Natural Science Foundation of China [grant Numbers 41322010 and 41571434].

References

Bao, A. N., A. M. Lechner, A. Fletcher, D. Mulligan, A. Mellor, and Z. Bai. 2012. "Comparison of Relative Radiometric Normalization Methods Using Pseudo-Invariant Features for Change Detection Studies in Rural and Urban Landscapes." *Journal of Applied Remote Sensing* 6 (10): 63578–63571. doi:10.1117/1.JRS.6.063578.

Bontemps, S., P. Bogaert, N. Titeux, and P. Defourny. 2008. "An Object-Based Change Detection Method Accounting for Temporal Dependences in Time Series with Medium to Coarse Spatial Resolution." *Remote Sensing of Environment* 112 (6): 3181–3191. doi:10.1016/j.rse.2008.03.013.

Bruzzone, L., and D. F. Prieto. 2000. "Automatic Analysis of the Difference Image for Unsupervised Change Detection." *IEEE Transactions on Geoscience & Remote Sensing* 38 (3): 1171–1182. doi:10.1109/36.843009.

Cao, G., Y. Li, Y. Liu, and Y. Shang. 2014. "Automatic Change Detection in High-Resolution Remote-Sensing Images by Means of Level Set Evolution and Support Vector Machine

Classification." *International Journal of Remote Sensing* 35 (16): 6255–6270. doi:10.1080/01431161.2014.951740.

Cao, G., L. Zhou, and Y. Li. 2016. "A New Change-Detection Method in High-Resolution Remote Sensing Images Based on A Conditional Random Field Model." *International Journal of Remote Sensing* 37 (5): 1173–1189. doi:10.1080/01431161.2016.1148284.

Celik, T. 2009. "Unsupervised Change Detection in Satellite Images Using Principal Component Analysis and *K*-Means Clustering." *IEEE Geoscience & Remote Sensing Letters* 6 (4): 772–776. doi:10.1109/LGRS.2009.2025059.

Chang, N. B., M. Han, W. Yao, L. C. Chen, and S. Xu. 2010. "Change Detection of Land Use and Land Cover in an Urban Region with SPOT-5 Images and Partial Lanczos Extreme Learning Machine." *Journal of Applied Remote Sensing* 4 (043551): 1–15. doi:10.1117/1.3518096.

Chen, Q., Y. Chen, and W. Jiang. 2016. "Genetic Particle Swarm Optimization-Based Feature Selection for Very-High-Resolution Remotely Sensed Imagery Object Change Detection." *Sensors* 16 (8): 1204. doi:10.3390/s16081204.

Conchedda, G., L. Durieux, and P. Mayaux. 2008. "An Object-Based Method for Mapping and Change Analysis in Mangrove Ecosystems." *ISPRS Journal of Photogrammetry and Remote Sensing* 63 (5): 578–589. doi:10.1016/j.isprsjprs.2008.04.002.

Coppin, P., I. Jonckheere, K. Nackaerts, B. Muys, and E. Lambin. 2004. "Digital Change Detection Methods in Ecosystem Monitoring: A Review." *International Journal of Remote Sensing* 25: 1565–1596. doi:10.1142/9789812777249_0001.

Deng, J. S., K. Wang, Y. H. Deng, and G. J. Qi. 2008. "PCA-Based Land-Use Change Detection and Analysis Using Multitemporal and Multisensory Satellite Data." *International Journal of Remote Sensing* 29 (16): 4823–4838. doi:10.1080/01431160801950162.

Desclée, B., P. Bogaert, and P. Defourny. 2006. "Forest Change Detection by Statistical Object-Based Method." *Remote Sensing of Environment* 102 (1): 1–11. doi:10.1016/j.rse.2006.01.013.

Du, P. J., and S. C. Liu. 2012. "Change Detection from Multi-Temporal Remote Sensing Images by Integrating Multiple Features." *Journal of Remote Sensing* 16 (4): 663–677. doi:10.11834/jrs.20121168.

Falco, N., M. D. Mura, F. Bovolo, J. A. Benediktsson, and L. Bruzzone. 2013. "Change Detection in VHR Images Based on Morphological Attribute Profiles." *IEEE Geoscience & Remote Sensing Letters* 10 (3): 636–640. doi:10.1109/LGRS.2012.2222340.

Foody, G. M. 2004. "Thematic Map Comparison: Evaluating the Statistical Significance of Differences in Classification Accuracy." *Photogrammetric Engineering and Remote Sensing* 70 (5): 627–634. doi:10.14358/PERS.70.5.627.

Gang, C., and G. J. Hay. 2011. "An Airborne Lidar Sampling Strategy to Model Forest Canopy Height from Quickbird Imagery and Geobia." *Remote Sensing of Environment* 115 (6): 1532–1542. doi:10.1016/j.rse.2011.02.012.

Ghosh, S., L. Bruzzone, S. Patra, F. Bovolo, and A. Ghosh. 2007. "A Context-Sensitive Technique for Unsupervised Change Detection Based on Hopfield-Type Neural Networks." *IEEE Transactions on Geoscience & Remote Sensing* 45 (3): 778–789. doi:10.1109/TGRS.2006.888861.

Ghosh, S., M. Roy, and A. Ghosh. 2014. "Semi-Supervised Change Detection Using Modified Self-Organizing Feature Map Neural Network." *Applied Soft Computing* 15 (3–4): 1–20. doi:10.1016/j.asoc.2013.09.010.

Gong, L., Q. Li, and J. Zhang. 2013. "Earthquake Building Damage Detection with Object-Oriented Change Detection." *Geoscience and Remote Sensing Symposium* 320 (17): 3674–3677. doi:10.1109/IGARSS.2013.6723627.

Hall, O., and G. J. Hay. 2003. "A Multiscale Object-Specific Approach to Digital Change Detection." *International Journal of Applied Earth Observation and Geoinformation* 4 (4): 311–327. doi:10.1016/S0303-2434(03)00010-2.

Hay, G. J., G. Castilla, M. A. Wulder, and J. R. Ruiz. 2005. "An Automated Object-Based Approach to the Multiscale Image Segmentation of Forest Scenes." *International Journal of Applied Earth Observation & Geoinformation* 7 (4): 339–359. doi:10.1016/j.jag.2005.06.005.

He, P., W. Shi, Z. Miao, H. Zhang, and L. Cai. 2015. "Advanced Markov Random Field Model Based on Local Uncertainty for Unsupervised Change Detection." *Remote Sensing Letters* 6 (9): 667–676. doi:10.1080/2150704X.2015.1054045.

Hegaratmascle, S. L., and R. Seltz. 2004. "Automatic Change Detection by Evidential Fusion of Change Indices." *Remote Sensing of Environment* 91 (3): 390–404. doi:10.1016/j.rse.2004.04.001.

Hu, Z., Z. Wu, Q. Zhang, Q. Fan, and J. Xu. 2013. "A Spatially-Constrained Color–Texture Model for Hierarchical VHR Image Segmentation." *IEEE Geoscience & Remote Sensing Letters* 10 (1): 120–124. doi:10.1109/LGRS.2012.2194693.

Huang, C., K. Song, S. Kim, J. R. G. Townshend, P. Davis, and J. G. Masek. 2008. "Use of a Dark Object Concept and Support Vector Machines to Automate Forest Cover Change Analysis." *Remote Sensing of Environment* 112 (3): 970–985. doi:10.1016/j.rse.2007.07.023.

Jian, P., K. Chen, and C. Zhang. 2016. "A Hypergraph-Based Context-Sensitive Representation Technique for VHR Remote-Sensing Image Change Detection." *International Journal of Remote Sensing* 37 (8): 1814–1825. doi:10.1117/12.2205593.

Johnson, B., and Z. Xie. 2011. "Unsupervised Image Segmentation Evaluation and Refinement Using a Multi-Scale Approach." *ISPRS Journal of Photogrammetry and Remote Sensing* 66 (4): 473–483. doi:10.1016/j.isprsjprs.2011.02.006.

Lefebvre, A., T. Corpetti, and L. Hubert-Moy 2008. "Object-Oriented Approach and Texture Analysis for Change Detection in Very High Resolution Images." *Geoscience and Remote Sensing Symposium* IEEE 4:IV–663. doi:10.1109/IGARSS.2008.4779809.

Li, J., and R. M. Narayanan. 2003. "A Shape-Based Approach to Change Detection of Lakes Using Time Series Remote Sensing Images." *IEEE Transactions on Geoscience & Remote Sensing* 41 (11): 2466–2477. doi:10.1109/TGRS.2003.817267.

Li, L., N. Shu, K. Wang, and Y. Gong. 2014. "Change Detection Method for Remote Sensing Images Based on Multi-Features Fusion." *Acta Geodaetica Et Cartographica Sinica* 43 (9): 945–953. doi:10.13485/j.cnki.11-2089.2014.0138.

Lo, C. P., and X. Yang. 2000. "Relative Radiometric Normalization Performance for Change Detection from Multi-Date Satellite Images." *Photogrammetric Engineering & Remote Sensing* 66 (8): 967–980.

Lu, D., P. Mausel, M. Batistella, and E. Moran. 2005. "Land-Cover Binary Change Detection Methods for Use in the Moist Tropical Region of the Amazon: A Comparative Study." *International Journal of Remote Sensing* 2005 (26): 101–114. doi:10.1080/01431160410001720748.

Möller, M., L. Lymburner, and M. Volk. 2007. "The Comparison Index: A Tool for Assessing the Accuracy of Image Segmentation." *International Journal of Applied Earth Observation and Geoinformation* 9 (3): 311–321. doi:10.1016/j.jag.2006.10.002.

Mountrakis, G., J. Im, and C. Ogole. 2011. "Support Vector Machines in Remote Sensing: A Review." *ISPRS Journal of Photogrammetry and Remote Sensing* 66 (3): 247–259. doi:10.1016/j.isprsjprs.2010.11.001.

Nackaerts, K., K. Vaesen, B. Muys, and P. Coppin. 2005. "Comparative Performance of a Modified Change Vector Analysis in Forest Change Detection." *International Journal of Remote Sensing* 26: 839–852. doi:10.1080/0143116032000160462.

Niemeyer, I., P. R. Marpu, and S. Nussbaum. 2008. "Change Detection Using Object Features." *Object-Based Image Analysis* 2008: 185–201. Springer Berlin Heidelberg.

Ojala, T., and M. Pietikäinen. 1999. "Unsupervised Texture Segmentation Using Feature Distributions." *Pattern Recognition* 32: 477–486. doi:10.1007/3-540-63507-6_216.

Ojala, T., M. Pietikäinen, and T. Mäenpää. 2002. "Gray-Scale and Rotation Invariant Texture Classification with Local Binary Patterns." *IEEE Transactions on Pattern Analysis & Machine Intelligence* 24: 971–987. doi:10.1007/3-540-45054-8_27.

Qin, R., X. Huang, A. Gruen, and G. Schmitt. 2015. "Object-Based 3-D Building Change Detection on Multi-Temporal Stereo Images." *IEEE Journal of Selected Topics in Applied Earth Observations & Remote Sensing* 8 (5): 1–13. doi:10.1109/JSTARS.2015.2424275.

Qin, Y., Z. Niu, F. Chen, B. Li, and Y. Ban. 2013. "Object-Based Land Cover Change Detection for Cross-Sensor Images." *International Journal of Remote Sensing* 34 (19): 6723–6737. doi:10.1080/01431161.2013.805282.

Rottensteiner, F., J. Trinder, S. Clode, and K. Kubik. 2005. "Using the Dempster-Shafer Method for the Fusion of Lidar Data and Multi-Spectral Images for Building Detection." *Information Fusion* 6 (4): 283–300. doi:10.1016/j.inffus.2004.06.004.

Ruthven, I., and M. Lalmas. 2002. "Using Dempster-Shafer's Theory of Evidence to Combine Aspects of Information Use." *Journal of Intelligent Information Systems* 19 (3): 267–301. doi:10.1023/A:1020114205638.

Singh, A. 1989. "Digital Change Detection Techniques Using Remotely Sensed Data." *International Journal of Remote Sensing* 10 (6): 989–1003. doi:10.1080/01431168908903939.

Tang, Y., L. Zhang, and X. Huang. 2011. "Object-Oriented Change Detection Based on the Kolmogorov-Smirnov Test Using High-Resolution Multispectral Imagery." *International Journal of Remote Sensing* 32 (20): 5719–5740. doi:10.1080/01431161.2010.507263.

Tian, J., P. Reinartz, P. D'Angelo, and M. Ehlers. 2013. "Region-Based Automatic Building and Forest Change Detection on Cartosat-1 Stereo Imagery." *ISPRS Journal of Photogrammetry & Remote Sensing* 79: 226–239. doi:10.1016/j.isprsjprs.2013.02.017.

Volpi, M., D. Tuia, F. Bovolo, M. Kanevski, and L. Bruzzone. 2013. "Supervised Change Detection in VHR Images Using Contextual Information and Support Vector Machines." *International Journal of Applied Earth Observation & Geoinformation* 20 (2): 77–85. doi:10.1016/j.jag.2011.10.013.

Wahler, R. A., and F. Y. Shih 1989. "Image Enhancement for Radiographs Utilizing Filtering, Gray Scale Transformation and Sobel Gradient Operator." *International Conference of the IEEE Engineering in Medicine and Biology Society*. IEEE 618-619. doi:10.1109/IEMBS.1989.95901.

Wang, B., S. Choi, Y. Byun, S. Lee, and J. Choi. 2015. "Object-Based Change Detection of Very High Resolution Satellite Imagery Using the Cross-Sharpening of Multi-Temporal Data." *IEEE Geoscience & Remote Sensing Letters* 12 (5): 1151–1155. doi:10.1109/LGRS.2014.2386878.

Wang, G. T., Y. L. Wang, and L. C. Jiao. 2010. "Change Detection Method of Multiband Remote Sensing Images Based on Fast Expectation-Maximization Algorithm and Fuzzy Fusion." *Journal of Infrared & Millimeter Waves* 29 (5): 383–388. doi:10.3724/SP.J.1010.2010.00383.

Wu, C., L. Zhang, and L. Zhang. 2016. "A Scene Change Detection Framework for Multi-Temporal Very High Resolution Remote Sensing Images." *Signal Processing* 124: 184–197. doi:10.1016/j.sigpro.2015.09.020.

Xian, G., and C. Homer. 2010. "Updating the 2001 National Land Cover Database Impervious Surface Products to 2006 Using Landsat Imagery Change Detection Methods." *Remote Sensing of Environment* 114 (8): 1676–1686. doi:10.1016/j.rse.2010.02.018.

Xiao, P., X. Zhang, D. Wang, M. Yuan, X. Feng, and M. Kelly. 2016. "Change Detection of Built-Up Land: A Framework of Combining Pixel-Based Detection and Object-Based Recognition." *ISPRS Journal of Photogrammetry & Remote Sensing* 119: 402–414. doi:10.1016/j.isprsjprs.2016.07.003.

Xu, H., L. Cheng, M. Li, Y. Chen, and L. Zhong. 2015. "Using Octrees to Detect Changes to Buildings and Trees in the Urban Environment from Airborne Lidar Data." *Remote Sensing* 7: 9682–9704. doi:10.3390/rs70809682.

Yang, Y., Q. Zhou, J. Gong, and Y. Wang. 2012. "An Integrated Spatio-Temporal Classification Method for Urban Fringe Change Detection Analysis." *International Journal of Remote Sensing* 33 (8): 2516–2531. doi:10.1080/01431161.2011.616551.

Yousif, O., and Y. Ban. 2016. "A Novel Approach for Object-Based Change Image Generation Using Multitemporal High-Resolution SAR Images." *International Journal of Remote Sensing* 2016: 1–23. doi:10.1080/01431161.2016.1217442.

Zhang, J., Q. Chen, Q. Sun, H. Sun, and D. Xia. 2011. "A Highly Repeatable Feature Detector: Improved Harris-Laplace." *Multimedia Tools & Applications* 52 (1): 175–186. doi:10.1007/s11042-010-0471-9.